1991

Impedance Analysis for Oxygen Reduction in a Lithium Carbonate Melt

Bhasker B. Davé
Texas A & M University - College Station

Ralph E. White
University of South Carolina - Columbia, white@cec.sc.edu

Supramaniam Srinivasan
Texas A & M University - College Station

A. John Appleby
Texas A & M University - College Station

Publication Info

Journal of the Electrochemical Society, 1991, pages 2675-2683.

When the same experiment is performed in SO_2Cl_2-solvate mixed electrolytes, this potential difference decreases to 570 mV. Figure 9b clearly indicates that the film is easier to remove in this electrolyte, since the first oxidation step occurs at a potential of 4.1 V against 4.4 V in SO_2Cl_2, $LiAlCl_4$ 2*M* electrolyte. That leads us to suppose that this first oxidation step is due to the oxidation of free chlorides, since Li^+ ions are tied up as complexes with the solvate, whereas free chloride ions do not exist in the SO_2Cl_2 pure electrolyte.

These results are in agreement with the previous data recorded by impedance measurements, pointing out the effect of the different morphology of the film obtained when solvate is present in the electrolyte.

Conclusions

Impedance measurements at a platinum microelectrode in SO_2Cl_2/solvate mixed electrolytes enable one to obtain information about the LiCl film formation during SO_2Cl_2 reduction. Difference of the morphology of this film is clearly demonstrated between the reduction made in pure SO_2Cl_2 or in the mixed SO_2Cl_2-solvate. The solvate allows one part of the LiCl produced during discharge to be complexed by the solvate. This yields a particular morphology of the passivating film. Indeed, the more aerated nature of the deposit obtained by adding solvate to SO_2Cl_2 allows the film to be easily removed by applying anodic potentials. Thus, we believe that the use of SO_2Cl_2-solvate mixed electrolytes would lead to more efficient charge-discharge cycles.

Acknowledgments

This work was supported by Direction des Recherches et Etudes Techniques no. 88160.

Manuscript submitted Dec. 26, 1990; revised manuscript received March 27, 1990.

SAFT assisted in meeting the publication costs of this article.

REFERENCES

1. C. R. Schlaikjer, in "Lithium Batteries," J. P. Gabano, Editor, p. 303, Academic Press, Inc., New York (1983).
2. D. L. Foster, H. C. Kuo, C. R. Schlaikjer, and A. N. Dey, *This Journal*, **135,** 2682 (1988).
3. A. N. Dey, H. C. Kuo, P. Piliero, and M. Kallianidis, *ibid.*, **135,** 2471 (1988).
4. D. L. Foster and H. C. Kuo, French Pat. 83 13038.
5. E. Lojou, R. Messina, J. Perichon, J. P. Descroix, and G. Sarre, *This Journal*, **136,** 293 (1989).
6. P. Chenebault, J. P. Planchat, and E. Lojou, in "Proceedings of 34th Power Sources Symposium 1990, To be published, IEEE.
7. M. Binder, S. Gilman, W. L. Wade, and C. W. Walker, *This Journal*, **131,** 1985 (1984).
8. S. Gilman and W. Wade, *ibid.*, **127,** 1427 (1980).
9. C. W. Walker, M. Binder, W. L. Wade and S. Gilman, *ibid.*, **132,** 1536 (1985).
10. K. A. Klinedinst, *ibid.*, **131,** 492 (1984).
11. E. Lojou, Ph.d. Thesis, Universitéde Paris XII (1988).
12. W. Hagans, N. Hampson and R. Racker, *Electrochim. Acta.*, **31,** 699 (1986).
13. A. Hills, N. Hampson, and M. Hayes, *J. Appl. Electrochem.*, **17,** 702 (1987).
14. M. C. Dhamelincourt, F. Wallart, P. Barbier, G. Mairesse, and J. P. Descroix, *J. Power Sources*, **14,** 77 (1985).
15. A. Le Mehaute and G. Crepy, *C. R. Acad. Sc., Paris*, t294, II 685 (1982).
16. A. Le Mehaute and G. Crepy, *Solid State Ionics*, **9-10,** 17 (1983).
17. A. Le Mehaute, A. De Guibert, M. Delahaye, and C. Filippi, *C. R. Acad. Sc., Paris*, t 294 II 835 (1982).
18. G. Crepy, CGE internal report.
19. M. Madou and S. Szpak, *This Journal*, **131,** 2471 (1984).
20. A. Meitav and E. Peled, *J. Electroanal. Chem.*, **134,** 49 (1982).
21. E. Lojou, R. Messina, J. Perichon, J. P. Descroix, and G. Sarre, *This Journal*, **136,** 299 (1989).
22. A. J. Hills, N. A. Hampson, and M. Hayes, *J. Electroanal. Chem.*, **209,** 351 (1986).
23. C. W. Walker, M. Binder, W. L. Wade, and S. Gilman, *This Journal*, **132,** 2817 (1985).

Impedance Analysis for Oxygen Reduction in a Lithium Carbonate Melt

Bhasker B. Davé*,[1] and Ralph E. White**

Center for Electrochemical Engineering, Department of Chemical Engineering, Texas A&M University, College Station, Texas 77843

Supramaniam Srinivasan and A. John Appleby****

Center for Electrochemical Systems and Hydrogen Research, Texas A&M University, College Station, Texas 77843

ABSTRACT

Oxygen reduction on a smooth gold electrode in a pure lithium carbonate melt was investigated by electrochemical impedance spectroscopy and cyclic voltammetry. The impedance data were analyzed using the Randles-Ershler equivalent circuit to determine parameters such as the charge-transfer resistance, Warburg coefficient, double-layer capacity, and uncompensated electrolyte resistance. The parameters estimated by complex plane plots and a complex nonlinear least squares method are in good agreement. Cyclic voltammetric measurements showed that oxygen reduction in a lithium carbonate melt is very rapid. A mass transfer parameter, $D_O^{1/2}C_O$, estimated by the cyclic voltammetry concurred with that calculated by the electrochemical impedance spectroscopy technique. The temperature dependences of the exchange current density and the product $D_O^{1/2}C_O$ were examined, and the apparent activation energies were determined to be 121.7 ± 24.4 and 181.0 ± 7.0 kJ/mol, respectively.

The oxygen reduction process in molten alkali carbonate electrolyte has been studied for the past quarter century because of its vital role in the performance and stability of the molten carbonate fuel cell. Appleby and Nicholson (1-4) examined the oxygen reduction reaction in molten carbonates on a submerged gold electrode using steady-state and potential scan techniques. They observed that oxygen reacts with carbonate ions and forms peroxide and superoxide ions and the concentrations of these species depend on the cations present in the melt. In a pure Li_2CO_3 or a Li-rich melt, the peroxide species is dominant, whereas in a K-rich melt the superoxide species is domi-

* Electrochemical Society Student Member.
** Electrochemical Society Active Member.
[1] Present address: Nalco Chemical Company, Naperville, Illinois 60563.

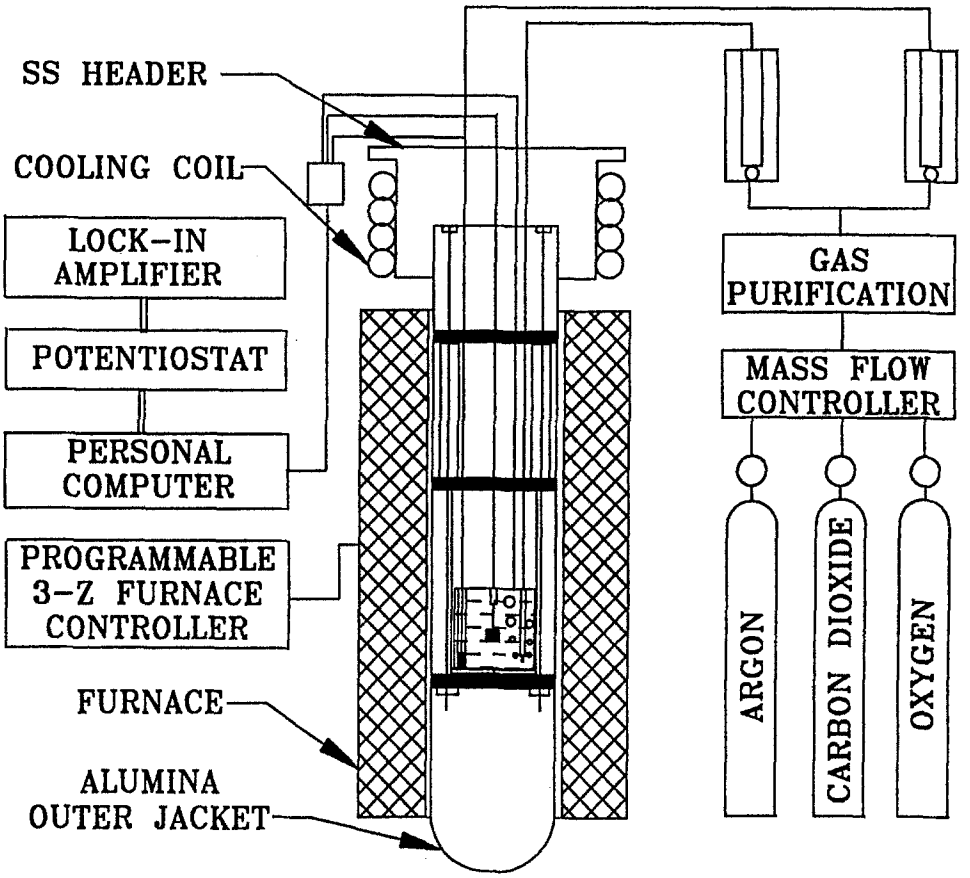

Fig. 1. Experimental setup for high-temperature electrode kinetic studies.

nant. Hence, the oxygen reduction mechanism strongly depends on the cations present in the melt. Andersen (5) carried out a thermodynamic study of the chemical equilibria in molten alkali carbonate electrolytes and demonstrated the presence of peroxide ions by quenching the melt followed by chemical analyses. Vogel *et al.* (6) studied the (Li-K)CO_3 eutectic melt at 650°C using a rotating gold wire and concluded that superoxide is dominant in this melt and presence of molecular oxygen in the melt is negligible. White and Twardoch (7) examined the (Li-Na-K)CO_3 eutectic melt at 680°C by cyclic voltammetry, chronopotentiometry, and chronoamperometry and observed the simultaneous presence of peroxide and oxide ions. Dunks and Stelman (8) studied pure sodium carbonate melt at 900°C and proposed the presence of percarbonate ions. Lu (9) investigated the oxygen reduction process in pure Li_2CO_3 and a Li-K (62:38 mole percent [m/o]) carbonate eutectic mixture using the potential step method. The exchange current density, determined by Lu (39 mA/cm^2 for 90% O_2 and 10% CO_2 at 750°C in pure Li_2CO_3 melt), is two orders of magnitude higher than that observed by Appleby and Nicholson (0.34 mA/cm^2), who used the potential scan technique. But the dependence of oxygen reduction kinetics on partial pressures of oxygen and carbon dioxide observed by Lu could not be explained by any of the mechanisms proposed in the literature. Uchida *et al.* (10) determined the kinetic parameters for oxygen reduction in a (Li-K)CO_3 (42.7:57.3 m/o) eutectic melt on a gold electrode using impedance analysis, potential step, and coulostatic relaxation methods. They found that the exchange current density was about the same order of magnitude as that observed by Lu. In addition, they concluded that impedance analysis is the most reliable of the three methods for the determination of the kinetic parameters for oxygen reduction in molten carbonates. Uchida *et al.* (11) examined the oxygen reduction on a lithiated NiO film, deposited on gold, and Sb-doped SnO_2 electrodes in Li-K eutectic melt by impedance spectroscopy and coulostatic relaxation techniques. They (12) also determined the temperature dependence of oxygen reduction kinetics on gold in (Li-K)CO_3 and determined the activation energies for the kinetic and mass-transfer related parameters. Recently, Adanuvor *et al.* (13) simulated the oxygen reduction reaction on a rotating disk electrode in various carbonate melts to examine the effect of dissolved gases on the electrode kinetics.

These studies show that (*i*) the oxygen reduction reaction in molten alkali carbonate strongly depends on the cations present in the melt; (*ii*) the reaction mechanism for the oxygen reduction in molten carbonate is not well understood; and (*iii*) the results reported in the literature are contradictory. Consequently, in the present work, we have used pure lithium carbonate melt to avoid the complexity of simultaneous presence of peroxide and superoxide ions. The oxygen reduction reaction on a submerged gold electrode is studied by electrochemical impedance spectroscopy (EIS) and cyclic voltammetry to determine the kinetic and transport parameters. Also, the influence of temperature on the oxygen reduction kinetics is examined, and the apparent activation energies are calculated.

Experimental

The experimental arrangement and the electrochemical cell assembly used for this work are shown in Fig. 1. The electrochemical cell was made of a recrystallized alumina cylinder of 99.8% purity, obtained from McDanel Company, with a capacity of about 90 cm^3. The working electrode was made of a submerged gold flag (0.0025 cm thick), with a geometrical area of one square centimeter, connected to the gold current collector (0.05 cm diam) by a thin gold wire to minimize the meniscus effect (2, 14), because the presence of a meniscus modifies the electrochemical response considerably (15, 16). The counterelectrode consisted of a large gold foil which was used as an inner liner of the cell to ensure uniform current distribution. The reference electrode was also made of a gold foil, but encased in an alumina tube which was pressed against the bottom of the electrochemical cell. The Puratronic grade (99.99%) gold foils and wires were obtained from Johnson Matthey/ÆSAR Group.

Digital mass flow controllers/meters manufactured by Teledyne-Hastings Raydist were used to provide the gas mixtures of the desired compositions of O_2, CO_2, and Ar, with high precision (±1% full scale). The high-purity gases

were obtained from Matheson Gas Products, and the traces of water were removed by passing the blended gas through a column of 5 Å molecular sieves and Drierite (Fisher Scientific). The gas mixture was bubbled into the melt in the vicinity of the working electrode at a flow rate of about 50 cm^3 min^{-1} through a long alumina tube with four pinholes to form smaller bubbles for enhanced mass transfer. The composition of the gas mixture supplied to the reference electrode compartment was the same as the one used for the working electrode, but at a flow rate of about 5 cm^3 min^{-1}.

The electrochemical cell was suspended from a stainless steel header using alumina tubings and an alumina bottom plate connected by the gold wires. Several pierced alumina baffles with spacers were used to decrease the convective heat-transfer in order to minimize the temperature gradient within the cell. Also, a three-zone furnace with individual microprocessor-based controllers (Applied Test Systems, Inc.) was used to ensure uniform temperature distribution in the cell. The cell temperature was monitored by a Chromel-Alumel thermocouple (Omega) enclosed in a closed-end alumina tube, which was firmly pressed against the bottom of the cell. The electrochemical cell and the hanging assembly was enclosed by an outer alumina jacket, held by the header using an O ring so that the electrochemical cell assembly was hermetically sealed. The stainless steel header also had a cooling coil to protect the O rings.

High-purity (99.999%) lithium carbonate (Alfa Products) was carefully weighed in an alumina crucible, and the electrochemical cell assembly was slowly heated (50°C/h) to 350°C under an inert (argon) environment. The electrochemical cell assembly was dried at 350°C in a carbon dioxide environment for 24 h before heating to 750°C.

The data acquisition setup consisted of a potentiostat/galvanostat (PAR Model 273), lock-in-amplifier (PAR Model 5301A), and personal computer (IBM PS/2). Software (PAR Headstart and Model 378) supplied by EG&G Princeton Applied Research was used for cyclic voltammetry and electrochemical impedance measurements. The wide range of frequency, from 0.05 Hz to 10 kHz, was used for the small signal perturbation, because the capacitive effect attributed to the double layer is significant at high frequency, whereas the mass-transfer related (Warburg) impedance is dominant at low frequency.

The impedance measurements for frequencies higher than 5 Hz were carried out by the phase sensitive detection (PSD) technique using the lock-in-amplifier and the potentiostat. In the PSD technique, the impedances are measured in the frequency domain; the voltage excitation signal is applied simultaneously to the electrochemical cell and a reference channel. The cell response (current signal) is compared with the perturbing signal, using a phase sensitive detector. Usually it is not possible to measure a cell impedance by the PSD technique with the excitation signal frequency below 1 Hz. Hence, for the perturbation signal of frequency below 5 Hz, the cell impedance was measured by the fast Fourier transform (FFT) technique using a personal computer and a potentiostat.

The FFT is a time domain technique in which a digitally generated pseudo-random white noise signal (*i.e.*, the algebraic sum of many individual waveforms of equal amplitude but having a different frequency and different phase characteristics) is used as a perturbing signal and the complex response to this signal is resolved by an inverse FFT into discrete frequency data. The FFT technique has a major advantage over frequency domain methods for low-frequency measurement because the data can be obtained considerably faster. The low-frequency measurements (below 5 Hz) reported here are an average of 15 data cycles in order to improve the accuracy of the data by averaging out the noise interference.

The amplitude of a perturbation signal needs to be small to ensure linear response of the electrochemical system, *i.e.*, to decrease the influence of higher harmonics on the measured impedance. The lower limit for the amplitude is determined by the signal-to-noise ratio which can be accepted by the measuring instrument, whereas the high limit is determined by the onset of nonlinear distortion (17). We compared the impedance spectra for oxygen reduction on gold in lithium carbonate melt at 750°C as a function of the excitation signal amplitude and observed that the effect of amplitude on the impedance spectra was insignificant when the amplitude of the perturbation signal was varied between 3 and 9 mV, indicating that measurements were in the linear domain. Hence, all the measurements reported here were obtained using an excitation signal amplitude of 5 mV. The impedance measurements were carried out at the equilibrium potential over the frequency range of 0.05 Hz to 10 kHz. The high-frequency measurements were limited to 10 kHz because an inductive behavior (positive imaginary impedance) was observed for frequency higher than 10 kHz.

Results and Discussion

Oxygen reduction reaction in lithium carbonate melt.—Cyclic voltammetry measurements obtained in a quiescent lithium carbonate melt as a function of scan rate for the gas composition of 90% O_2 and 10% CO_2 at 850°C are shown in Fig. 2. The potential scans were carried out between the rest potential (0.0 V) of the working electrode and −0.5 V *vs.* the reference electrode. The scan rates were varied from 10 to 200 mV/s. During the forward scan, a diffusion-limited peak, followed by a limiting plateau, was observed. Appleby and Nicholson (2) studied the oxygen reduction reaction in lithium carbonate using potential sweep and steady-state techniques; they made a similar observation and proposed the following mechanism

$$1/2\ O_2 + CO_3^{2-} \rightleftharpoons O_2^{2-} + CO_2 \quad [1]$$

$$O_2^{2-} + e^- \rightleftharpoons (O^-) + O^{2-} \quad [2]$$

$$(O^-) + CO_2 + e^- \rightleftharpoons CO_3^{2-} \quad [3]$$

$$O^{2-} + CO_2 \rightleftharpoons CO_3^{2-} \quad [4]$$

$$1/2\ O_2 + CO_2 + 2e^- \rightleftharpoons CO_3^{2-} \quad [5]$$

They concluded that for oxygen reduction on a submerged gold electrode, the first electron transfer step (Eq. [2]) may be the rate-determining step, although in a molten carbonate fuel cell, the recombination reaction (Eq. [4]) could be slower, and the oxygen reduction process could be mass-transfer limited in a porous electrode. As shown in Fig. 2, the peak potential was 40-50 mV negative of the rest potential and did not vary with the scan rate of up to 200 mV/s; this behavior was also observed by Lu (9) and Uchida *et al.* (10) in (Li-K) carbonate eutectic melt.

Impedance measurements and analysis.—The impedance measurements were carried out at the equilibrium potential with a sinusoidal perturbation signal of 5 mV amplitude and the frequency range of 0.05 Hz to 10 kHz. The complex-plane plot for the impedances measured at 750°C and 90% O_2 and 10% CO_2 gas composition is shown in Fig. 3. The absence of a semicircle in the complex plane plot indicates fast electrode kinetics (18). In the region of

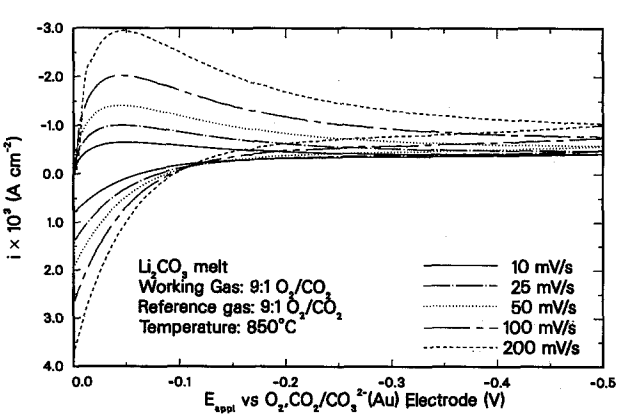

Fig. 2. Effect of scan rate on the cyclic voltammogram for oxygen reduction on a submerged gold electrode in lithium carbonate melt at 850°C.

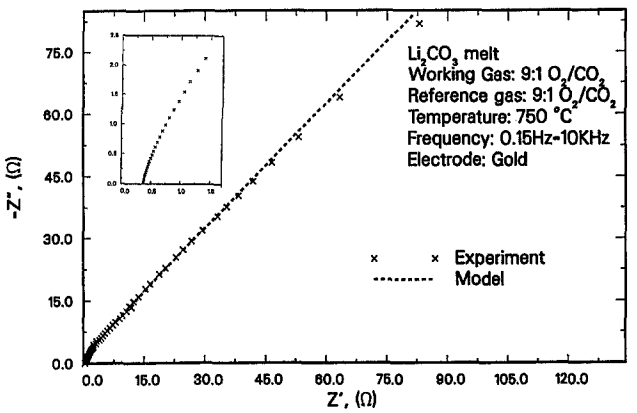

Fig. 3. Complex plane plots for impedance spectrum measured at the rest potential and 750°C. The figure inset is a magnified plot for the high-frequency data.

low frequency, the complex plane impedance plot shows a linear behavior with slope of 45° due to the mass-transfer-related (Warburg) impedance (19). The complex-plane plot for frequencies higher than 100 Hz is shown in the inset in Fig. 3. In the region of high frequency, the imaginary part of the impedance (Z'') diminished with increasing frequency, and at about 10 kHz approached zero.

The impedance analysis was carried out by using the equivalent circuit model shown in Fig. 4. This model is called the Randles-Ershler equivalent circuit model (20, 21) and consists of two parallel paths for the two parallel processes occurring at the electrode-electrolyte interface. These processes are double-layer charging and the faradaic charge transfer. The faradaic impedance consists of the charge-transfer resistance and the diffusional impedance in series. The uncompensated resistance between the reference and the working electrodes is given by R_s, which is connected in series with the rest of the circuit.

Impedance analysis by the Randles-Ershler equivalent circuit model is based on the following assumptions (17, 22, 23): (*i*) linearized current-potential characteristic is applicable because the amplitude of the sinusoidal perturbation signal is small (so that the higher harmonic response, due to the dependence of the double-layer capacitance on a voltage across the interface and the exponential dependence of the faradaic current on the surface overpotential, is negligible) and the impedance measurements were made at the equilibrium potential of the working electrode; (*ii*) semi-infinite boundary condition for the mass transfer (*i.e.*, in the region far away from the electrode, the bulk concentrations of the species are unperturbed); (*iii*) uniform current distribution on a planar working electrode (*i.e.*, the working electrode is large enough so that deviations from homogeneity of the electric field at the edges is negligible and the counterelectrode completely surrounds the working electrode); (*iv*) *a priori* separation of the faradaic process and the double-layer structure (*i.e.*, the faradaic impedance and the double-layer reactance are independent of each other); (*v*) the mass transfer is due to diffusion only (*i.e.*, negligible influence of migration and convection); (*vi*) frequency dispersion of the double-layer capacitance is negligible; and (*vii*) charge transfer takes place at the interface in the absence of specific adsorption.

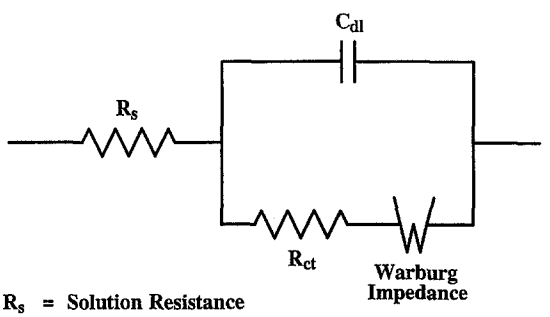

Fig. 4. The Randles-Ershler equivalent circuit model to represent the interfacial impedance for oxygen reduction on gold in lithium carbonate melt.

The expressions for the real (Z') and the imaginary (Z'') part of the total impedance (Z) are as follows (23)

$$Z = R_s + \frac{1}{[(R_{ct} + Z_W)^{-1} + j\omega C_{dl}]} = Z' - jZ'' \quad [6]$$

where

$$Z' = R_s + \frac{R_{ct} + \sigma\sqrt{\omega}}{(C_{dl}\sigma\sqrt{\omega} + 1)^2 + \omega^2 C_{dl}^2 (R_{ct} + \sigma/\sqrt{\omega})^2} \quad [7]$$

$$Z'' = \frac{\omega C_{dl}(R_{ct} + \sigma/\sqrt{\omega})^2 + \sigma/\sqrt{\omega}(C_{dl}\sigma\sqrt{\omega} + 1)}{(C_{dl}\sigma\sqrt{\omega} + 1)^2 + \omega^2 C_{dl}^2 (R_{ct} + \sigma/\sqrt{\omega})^2} \quad [8]$$

Impedance analysis based on the Randles-Ershler equivalent circuit model yields estimates for four parameters, namely, the charge-transfer resistance (R_{ct}), double-layer capacity (C_{dl}), Warburg coefficient (σ), and solution resistance (R_s).

Impedance analysis using complex plane plots.—The uncompensated solution resistance was determined to be 0.38 Ω for the impedance spectrum shown in Fig. 3 by the high-frequency limits of Eq. [7] and [8]

As $\omega \to \infty$

$$Z' = R_s \quad [9]$$

$$Z'' = 0 \quad [10]$$

The charge-transfer resistance, Warburg coefficient, and double-layer capacity were determined by the frequency variation of impedance and admittance spectra in a low-frequency region.

As $\omega \to 0$, the Eq. [7] and [8] approach the following limit forms

$$Z' = R_s + R_{ct} + \sigma/\sqrt{\omega} \quad [11]$$

$$Z'' = \sigma/\sqrt{\omega} + 2\sigma^2 C_{dl} \quad [12]$$

Using Eq. [11], the Warburg coefficient (σ) was calculated to be 82.5 Ω cm^2 s$^{-1/2}$ from the slope of a Z' *vs.* $\omega^{-1/2}$ plot in the low-frequency region (0.15-30 Hz), which is shown in Fig. 5. By substituting Eq. [12] into Eq. [11], we get

$$Z'' = Z' - R_s - R_{ct} + 2\sigma^2 C_{dl} \quad [13]$$

The complex plane plot for impedance data in a low-frequency region is shown in Fig. 6; the slope of this plot is equal to unity, and the intercept is expressed by

$$\text{Intercept} = -R_s - R_{ct} + 2\sigma^2 C_{dl} \quad [14]$$

Since the uncompensated solution resistance is already determined from the high-frequency limits, the interfacial admittance (Y_{el}) can be expressed by the following expressions

$$Y_{el} = Y_{el}' + jY_{el}'' \quad [15]$$

$$Y_{el}' = \frac{Z' - R_s}{(Z' - R_s)^2 + (Z'')^2} \quad [16]$$

$$Y_{el}'' = \frac{Z''}{(Z' - R_s)^2 + (Z'')^2} \quad [17]$$

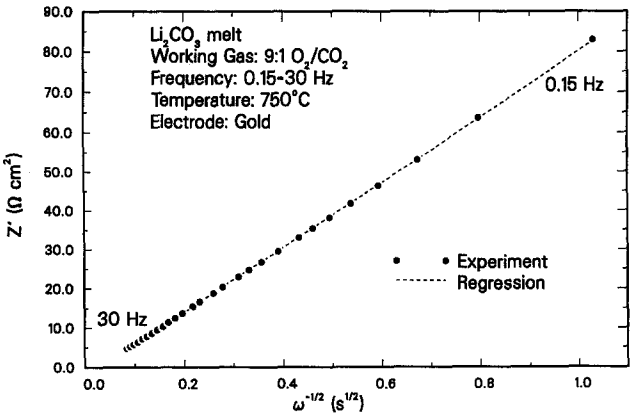

Fig. 5. Plot of Z′ *vs.* $\omega^{-1/2}$ for estimation of the Warburg coefficient.

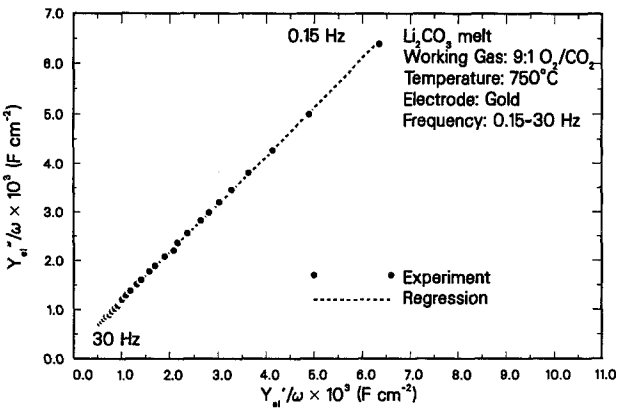

Fig. 7. Plot of Y_{el}''/ω *vs.* Y_{el}'/ω for the determination of the double-layer capacity.

By substituting Eq. [7] and [8] into Eq. [16] and [17], and using a parameter $p = R_{ct}/\sigma\omega^{-1/2}$

$$Y_{el}' = \frac{\omega^{1/2}}{\sigma}\frac{p+1}{p^2+2p+2} \quad [18]$$

$$Y_{el}'' = \frac{\omega^{1/2}}{\sigma}\frac{1}{p^2+2p+2} + \omega C_{dl} \quad [19]$$

By substituting Eq. [18] into Eq. [19]

$$Y_{el}'' = \frac{Y_{el}'}{p+1} + \omega C_{dl} \quad [20]$$

The parameter p plays an important role in the separation of charge-transfer resistance from the Warburg coefficient because it indicates the mode of control over the faradaic impedance: charge-transfer resistance is dominant when $p \rightarrow \infty$ and mass-transfer (Warburg) impedance is controlling when $p \rightarrow 0$ (21). Hence, p is much less than 1 in the low-frequency region where the mass-transfer-related impedance is dominant, and Eq. [20] can be approximated by the following expression

$$\frac{Y_{el}''}{\omega} = \frac{Y_{el}'}{\omega} + C_{dl} \quad [21]$$

As shown in Fig. 7, a plot of Y_{el}''/ω *vs.* Y_{el}'/ω showed a linear behavior with a slope of 45°, and the double-layer capacitance was determined to be 276 μF cm^{-2} from the intercept. The charge-transfer resistance was calculated to be 0.95 Ω cm^2, by substituting the values of σ, R_s, and C_{dl} into Eq. [14]. The parameters estimated by this technique are given in Table I.

Impedance data analysis by nonlinear parameter estimation.—A complex nonlinear least squares (CNLS) parameter estimation program (24-26) was used with the Randles-Ershler equivalent circuit model (Eq. [7] and [8]) to analyze the impedance spectrum to determine kinetic and mass-transfer-related parameters. The objective function for minimization is described below

$$f(\mathbf{X}) = \sum_{i=1}^{N} [w_i'(Z'_{exp,i} - Z'_{mod,i})^2 + w_i''(Z''_{exp,i} - Z''_{mod,i})^2] \quad [22]$$

In our analysis, we found that the weighting factor (inverse of the error variance) considerably influenced the accuracy of the parameters estimated from the impedance data (27). Here, we have used the proportional and functional proportional weighting factors (28) to estimate the charge-transfer resistance, double-layer capacity, and Warburg coefficient from the impedance data. As shown in the complex plane plot in Fig. 3, the model impedance data, calculated using the estimated parameters and the Randles-Ershler equivalent circuit model (Eq. [7] and [8]), were consistent with the experimental data. Since the impedance measurements were obtained at the equilibrium potential, the charge-transfer resistance can be expressed as follows (21)

$$R_{ct} = \frac{RT}{nFi_o} \quad [23]$$

The exchange current density for the oxygen reduction reaction on a gold electrode was calculated to be 44.0 mA cm^{-2} by using Eq. [23]. As shown in Table I, the parameters estimated by the complex plane plot methods and the CNLS technique compare well. The complex plane plot technique utilizes the impedance data in a low-frequency region only, whereas the computer curve fitting (CNLS) method uses the entire impedance spectrum. Hence, the parameters estimated by the CNLS technique have better accuracy than those obtained by the complex plane plots.

Influence of temperature.—Temperature dependence of the oxygen reduction reaction in lithium carbonate melt was investigated by electrochemical impedance spectroscopy to determine the activation energies of the exchange current density and the Warburg coefficient. The effect of temperature on a plot of phase angle *vs.* log ω is shown in Fig. 8. In the high-frequency region, all plots converged to

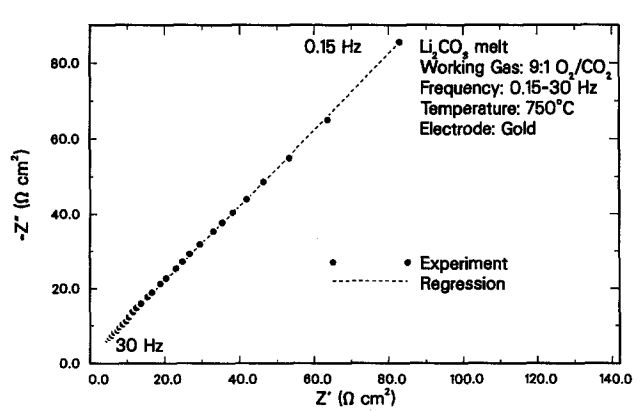

Fig. 6. The complex plane plot for the impedance data measured in a low-frequency region to determine the charge-transfer resistance.

Table I. Comparison of kinetic and mass-transfer parameters estimated by complex plane plots and complex nonlinear least squares technique: temperature 750°C; gas composition 90% O_2 and 10% CO_2.

Method	σ (Ω cm^2 s$^{-1/2}$)	R_{ct} (Ω cm^2)	C_{dl} (μF cm^{-2})	R_s (Ω cm^2)
Complex plane plots	82.5	0.95	276	0.38
CNLS	81.3 ± 2.5	0.95 ± 0.48	301 ± 17	0.38

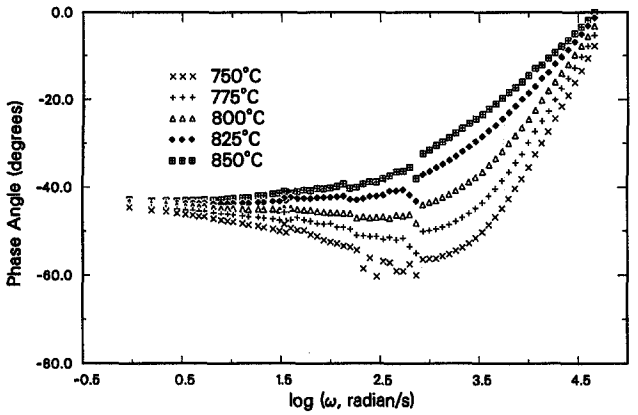

Fig. 8. Effect of temperature on a phase angle *vs.* log ω plot for O_2 reduction on gold electrode in Li_2CO_3 melt at 0.9 atm P_{O_2} and 0.1 atm P_{CO_2}.

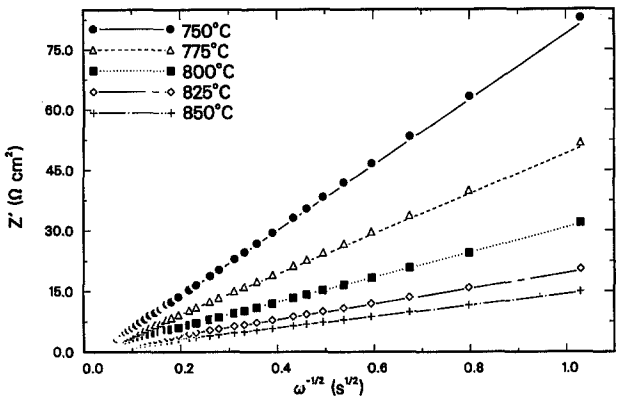

Fig. 9. Effect of temperature on Z′ *vs.* $\omega^{-1/2}$ plot for O_2 reduction on a gold electrode in Li_2CO_3 melt at 0.9 atm P_{O_2} and 0.1 atm P_{CO_2}. Symbols: experimental data. Lines: regression data.

a 0° phase angle indicating that the solution resistance becomes dominant. At frequencies below 30 Hz, the phase angle approached −45°, indicating mass-transfer impedance was significant. The impedance spectra obtained as a function of temperature were analyzed by the CNLS method, and the optimized parameters are given in Table II. The effect of temperature on Z′ *vs.* $\omega^{-1/2}$ plot is shown in Fig. 9. In the low-frequency region, Fig. 9 shows a linear behavior of Z′ *vs.* $\omega^{-1/2}$ indicating that the mass-transfer impedance is dominant. The Warburg coefficient (Eq. [11]) is proportional to the slope of the lines in Fig. 9. The lines in Fig. 9 indicate that an increase in the temperature decreased the Warburg coefficient. This observation is corroborated, quantitatively, by the estimated parameters shown in Table II. An increase in temperature from 750 to 850°C caused more than a fivefold decrease in the Warburg coefficient, whereas the decrease in the charge-transfer resistance was about threefold. The double-layer capacity value increased with the increase in temperature; a similar trend was observed when the partial pressure of oxygen was increased, while the partial pressure of carbon dioxide was kept constant (29). The increase in double-layer capacity with temperature may have been due to the formation of a solid oxide film on a gold electrode. The effects of temperature on the entire impedance spectrum can be observed by log |Z| *vs.* log ω plots in Fig. 10. In the high-frequency region, log |Z| *vs.* log ω plot approached the uncompensated electrolyte resistance, R_s, which is independent of frequency. In the low-frequency region, complete relaxation due to the charge-transfer process ($R_{ct}C_{dl}$) is not observed due to the Warburg impedance. As shown in Fig. 10, the experimental and model data were in good harmony for the entire frequency range of the experiment.

Since impedance measurements were obtained at the equilibrium potential, in the absence of dc polarization, the Warburg coefficient is expressed by the following equation (21)

$$\sigma = \frac{RT}{n^2F^2A\sqrt{2}}\left(\frac{1}{D_O^{1/2}C_O} + \frac{1}{D_R^{1/2}C_R}\right) \qquad [24]$$

For oxygen reduction in lithium carbonate melt, the concentration of the peroxide ions (C_O) is much smaller than the concentration of the carbonate ions (C_R). Considering that D_O and D_R are of the same order of magnitude, then $1/D_R^{1/2}C_R$ is negligible compared with $1/D_O^{1/2}C_O$. Thus, Eq. [24] can be approximated by the following expression

$$\sigma = \frac{RT}{n^2F^2A\sqrt{2}}\left(\frac{1}{D_O^{1/2}C_O}\right) \qquad [25]$$

The mass-transfer parameter, $D_O^{1/2}C_O$, and the exchange current density values were calculated using Eq. [25] and [23], respectively. The Arrhenius plot for the exchange current density is shown in Fig. 11, and the activation energy was estimated to be 121.7 ± 24.4 kJ mol^{-1}. The apparent activation energy for the mass-transfer parameter, $D_O^{1/2}C_O$, was calculated to be about 181.0 ± 7.0 kJ mol^{-1}, and the Arrhenius plot for it is shown in Fig. 12. The apparent activation energy for the mass-transfer parameter is a sum of the activation energy for the formation of peroxide ions (Eq. [1]) and one half of the activation energy of its diffusion coefficient. The estimated activation energy value for $D_O^{1/2}C_O$ is very close to that determined by Appleby and Nicholson (2) for oxygen reduction in lithium carbonate melt. Uchida *et al.* (12) examined the effect of temperature on oxygen reduction on a submerged gold electrode in (Li-K)CO_3 and observed a remarkable change in these activation energies with temperature. This change in activation energy with temperature indicates a shift in the rate-controlling mechanism of oxygen reduction. The activation energies determined by Uchida *et al.* (12) in the region of temperature higher than 700°C were about 110 and 149 kJ/mol for i_o and $D_O^{1/2}C_O$, respectively. These values are close to the values obtained in this work for oxygen reduction in lithium carbonate melt, which is known to proceed via peroxide mechanism. Also, the study conducted by Uchida *et al.* showed that the activation energies increased

Table II. Parameters estimated by impedance analysis using CNLS program: gas composition 90% O_2 and 10% CO_2; parameter R_s, constant parameter.

Temperature (°C)	σ (Ω cm² $s^{-1/2}$)	R_{ct} (Ω cm²)	C_{dl} (μF cm^{-2})	R_s (Ω cm²)
750	81.3 ± 2.5	0.95 ± 0.48	301 ± 17	0.38
775	49.8 ± 2.0	0.93 ± 0.35	400 ± 26	0.38
800	30.6 ± 1.0	0.68 ± 0.17	506 ± 29	0.38
825	19.2 ± 0.6	0.40 ± 0.10	692 ± 42	0.38
850	13.9 ± 0.3	0.30 ± 0.05	855 ± 44	0.39

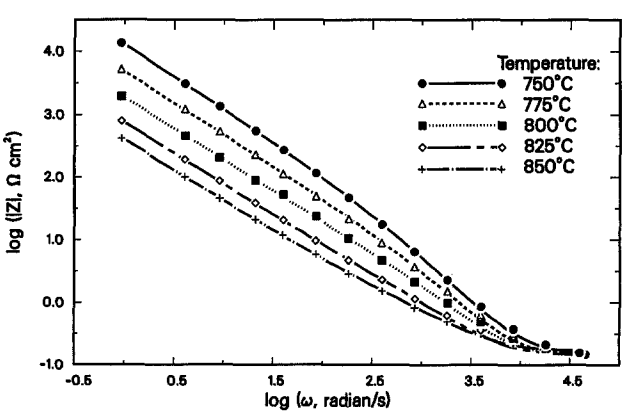

Fig. 10. Effect of temperature on log |Z| vs. log ω plot for O_2 reduction on gold electrode in Li_2CO_3 melt at 0.9 atm P_{O_2} and 0.1 atm P_{CO_2}. Symbols: experimental data. Lines: regression data.

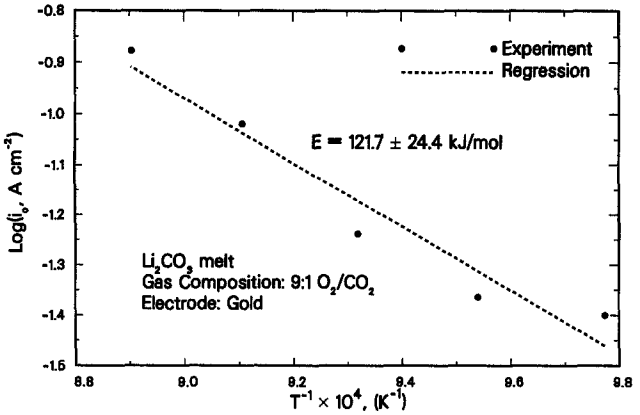

Fig. 11. Arrhenius plot for the exchange current density, determined by impedance analysis.

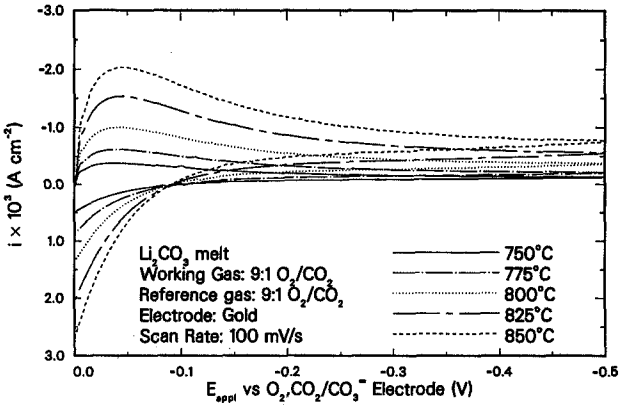

Fig. 13. Effect of temperature on cyclic voltammogram for O_2 reduction; reference and working gases have the same composition.

with temperature, indicating that the rate-controlling mechanism has shifted to an alternate or parallel path (30). If the controlling mechanism had shifted from one of a succession of elementary steps to another in the series, then the activation energy for i_o would have decreased with the increase in temperature. These results indicated that the oxygen reduction in (Li-K)CO_3 eutectic melt at temperatures higher than 700°C proceeded via peroxide mechanism. The other rate-controlling mechanism, for temperatures below 700°C, could be the superoxide mechanism.

Cyclic voltammetry.—Cyclic voltammetry was carried out to study the effect of temperature on oxygen reduction on a submerged gold electrode in lithium carbonate melt for the gas composition of 90% O_2 and 10% CO_2. The effect of temperature on cyclic voltammogram for the scan rate of 100 mV/s is shown in Fig. 13. As shown in Fig. 13, an increase in temperature increased the cathodic peak current density. The current densities in the reverse scan were less cathodic than those obtained in the forward scan, and there was no peak reversal. When the applied potential returned to the initial potential, a large anodic current was observed which subsided slowly and reached zero in a few minutes. Since the cyclic voltammograms shown in Fig. 13 are for the same scan rate of 100 mV/s, the area under the cathodic sweep represented the charge passed during the forward sweep. A plot of the anodic current density, observed at the end of the sweep, *vs.* the charge passed in the forward sweep showed a linear behavior with a slope of about 0.5, when the potential scan rate was kept constant at 100 mV/s and temperature was varied from 750 to 850°C. Lu (9) made a similar observation for oxygen reduction on gold in a eutectic mixture of lithium carbonate and potassium carbonate. He attributed this behavior to the local accumulation of unneutralized oxide ions, which shifts the reversible electrode potential in the negative direction. As suggested by Borucka (31) the reversible electrode (O_2, CO_2/CO_3^{2-}) potential may depend on the local activity of oxide ion at the electrode-electrolyte interface

$$E_{O_2,CO_2/CO_3^{2-}} = E^{\circ}_{O_2/O^{2-}} + \frac{RT}{2F} \ln \left(\frac{P_{O_2}^{1/2}}{a_{O^{2-}}} \right) \qquad [26]$$

where

$$E^{\circ}_{O_2/O^{2-}} = E^{\circ}_{O_2,CO_2/CO_3^{2-}} + \frac{RT}{2F} \ln K_d \qquad [27]$$

Lu and Selman (32) showed that oxygen electrode potential shifts in the negative direction by the addition of lithium oxide to the melt. As shown in Fig. 13, the peak potential was about 45-50 mV negative of the reversible potential, which corresponded to RT/nF (n = 2 for peroxide reduction). The peak current density *vs.* square root of the scan rate plots for various temperatures are shown in Fig. 14. The linear behavior of i_p *vs.* $v^{1/2}$ plots, shown in Fig. 14, and invariance of E_p with respect to the scan rate (up to 200 mV/s) indicated that oxygen reduction in lithium carbonate melt has fast kinetics (33). Similar behavior was observed by Lu (9) and Uchida *et al.* (10) in the eutectic mixture of lithium carbonate and potassium carbonate. The slope of i_p *vs.* $v^{1/2}$ plot is proportional to the concentration of the diffusing species. As suggested by Appleby and Nicholson (2), the diffusion-limited peak for O_2 reduction in Li_2CO_3 can be described by the theory developed by Berzins and Delahay (34) for the reversible diffusion-controlled peak where the product activity is considered to be invariant and equal to unity (*e.g.*, metal deposition), because the final product of the oxygen reduction in molten carbonate is the carbonate ion (Eq. [5]). The expression for the peak current density is similar to the one for the polarographic case, except that the numerical coefficient is different. The proportionality between the peak current den-

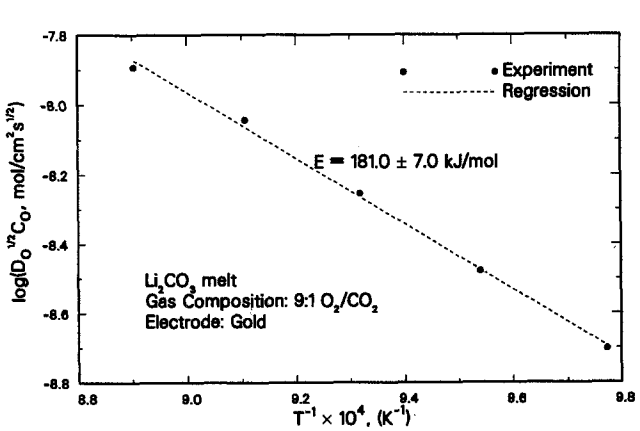

Fig. 12. Arrhenius plot for the product, $D_O^{1/2}C_O$, estimated by impedance analysis.

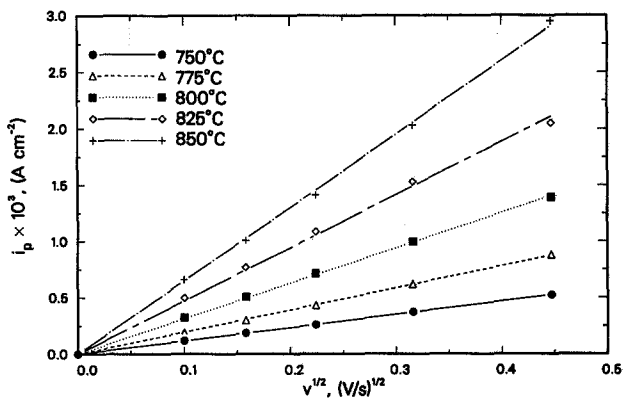

Fig. 14. Effect of temperature on i_p *vs.* $v^{1/2}$ plot for O_2 reduction on gold electrode in Li_2CO_3 melt at 0.9 atm P_{O_2} and 0.1 atm P_{CO_2}. Symbols: experimental data. Lines: regression data.

Table III. Comparison of product, $D_O^{1/2}C_O$, estimated by cyclic voltammetry and impedance analysis: gas composition 90% O_2 and 10% CO_2.

Temperature (°C)	$D_O^{1/2}C_O \times 10^9$ mol cm^{-2} s$^{-1/2}$	
	Cyclic voltammetry	Impedance analysis
750	2.09	1.99 ± 0.03
775	3.50	3.33 ± 0.06
800	5.73	5.53 ± 0.09
825	8.70	9.01 ± 0.13
850	12.14	12.70 ± 0.14

sity and the concentration of the diffusing species is given below

$$i_p = 0.61(nF/RT)^{1/2}nFD_O^{1/2}C_O v^{1/2} \quad [28]$$

The mass-transfer parameter, $D_O^{1/2}C_O$, was calculated from the slope of i_p *vs.* $v^{1/2}$ by using Eq. [28]. As shown in Table III, the values of $D_O^{1/2}C_O$ obtained by cyclic voltammetry concurred well with those estimated by the electrochemical impedance spectroscopy. The product, $D_O^{1/2}C_O$, increased with the increase in temperature, which is partly due to the increase in peroxide ion concentration. The apparent activity energy for $D_O^{1/2}C_O$ obtained by cyclic voltammetry was about 170 kJ/mol, which is consistent with the value obtained by electrochemical impedance spectroscopy.

Conclusions

The oxygen reduction reaction on a submerged gold electrode in a pure lithium carbonate melt was examined by electrochemical impedance spectroscopy and cyclic voltammetry techniques. The cyclic voltammogram showed a diffusion-limited peak followed by a limiting current plateau. The peak potential did not vary with the scan rate, and the peak potential was ~45 mV ($RT/2F$) negative of the equilibrium potential, indicating that the oxygen reduction in a pure lithium carbonate melt involves two electrons. The linear variation of the peak current density with the square root of the scan rate and invariance of the peak potential with respect to the scan rate showed that oxygen reduction in a pure lithium carbonate melt is "reversible" up to 200 mV/s.

Since the complex plane impedance plot did not show a semicircular relaxation, the electrochemical impedance spectrum indicates that electrode kinetics of oxygen reduction reaction in a pure lithium carbonate melt is very rapid. In a region of low frequency, the complex plane impedance plot showed a linear behavior with a slope of 45°, indicating that the diffusional process is dominant. The impedance spectra were analyzed by the complex plane plots and the complex nonlinear least squares methods to determine the kinetic and mass-transfer parameters such as the charge-transfer resistance, Warburg coefficient, double-layer capacity, etc. The electrode kinetic and mass-transfer parameters determined by the complex plane plots and CNLS program agreed well. The parameters obtained by CNLS technique are expected to have better accuracy than those obtained by complex plane plots, and this technique also provides the confidence limits for the estimated parameters.

The electrode kinetic and mass-transfer parameters for the oxygen reduction reaction were determined as functions of temperature. The Warburg coefficient (impedance due to mass transfer) decreased with an increase in temperature; this effect can be attributed to the increase in concentration and diffusion coefficient of peroxide species with temperature. The charge-transfer resistance also decreased with an increase in temperature. The apparent activation energies for the exchange current density and mass-transfer parameter, $D_O^{1/2}C_O$, were determined to be 121.7 ± 24.4 and 181.0 ± 7.0 kJ/mol, respectively. The mass-transfer parameters estimated by electrochemical impedance spectroscopy and cyclic voltammetry techniques showed good agreement. The double-layer capacitance value for a gold electrode in Li_2CO_3 melt was estimated to be 301 ± 17 μF cm^{-2} at 750°C, which is higher than that observed in the aqueous electrolytes.The double-layer capacitance also increased with an increase in temperature. This effect is difficult to explain, since very little information about the double-layer structure in molten carbonate electrolytes is available in the literature.

Acknowledgment

Financial support for this project from the U.S. Department of Energy (Contract No. DE-FG22-87PC79931) and Electric Power Research Institute (Contract No. RP8002-7) is gratefully acknowledged. The authors would like to thank Professor J. R. Selman for helpful suggestions and Professor J. R. Macdonald for suggestions on impedance analysis and providing the CNLS program.

Manuscript submitted Sept. 5, 1990; revised manuscript received March 14, 1991.

Texas A&M University assisted in meeting the publication costs of this article.

LIST OF SYMBOLS

A	electrode area, cm^2
C_{dl}	double-layer capacitance, μF/cm^2
C_j	bulk concentration of species j, mol/cm^3
D_j	bulk diffusion coefficient of species j, cm^2/s
E_p	peak potential, V
F	Faraday's constant, 96,487 C/equiv.
f	objection function for minimization, Ω cm^2
i	current density, A/cm^2
i_o	exchange current density, A/cm^2
i_p	peak current density, A/cm^2
K_d	decomposition constant for lithium carbonate
n	number of electrons transferred in electrode reaction
N	total number of observations
P	pressure, atm
R	universal gas constant, 8.3143 J mol^{-1} K^{-1}
R_{ct}	charge-transfer resistance, Ω cm^2
R_s	solution resistance, Ω cm^2
t	time, s
T	temperature, K
v	scan rate, mV/s
w	weighting factor
$\mathbf{X}$	vector of model parameters
Y_{el}	interfacial admittance, Ω^{-1} cm^{-2}
Z	impedance, Ω cm^2
$\|Z\|$	modulus of impedance, Ω cm^2
Z_W	Warburg impedance, Ω cm^2

Greek letters

β	symmetry factor for electrochemical reaction
σ	Warburg coefficient, Ω cm^2 s$^{-1/2}$
ϕ	phase angle
ω	angular frequency, radian/s

Superscripts

′	real part
″	imaginary part

Subscripts

i	ith measurement point
O	peroxide ions
R	carbonate ions

REFERENCES

1. A. J. Appleby and S. B. Nicholson, *J. Electroanal. Chem.*, **38,** App. 14 (1972).
2. A. J. Appleby and S. B. Nicholson, *ibid.*, **53,** 105 (1974).
3. A. J. Appleby and S. B. Nicholson, *ibid.*, **83,** 309 (1977).
4. A. J. Appleby and S. B. Nicholson, *ibid.*, **112,** 71 (1980).
5. B. Kr. Andersen, Ph.D. Dissertation, The Technical University of Denmark, Lyngby, Denmark (1975).
6. W. M. Vogel, S. W. Smith, and L. J. Bregoli, *This Journal*, **130,** 575 (1983).
7. S. H. White and U. M. Twardoch, *Electrochim. Acta*, **27,** 1599 (1982).
8. G. B. Dunks and D. Stelman, *Inorg. Chem.*, **22,** 2168 (1983).
9. S. H. Lu, Ph.D. Dissertation, Illinois Institute of Technology, Chicago, IL (1985).
10. I. Uchida, T. Nishina, Y. Mugikura, and K. Itaya, *J. Electroanal. Chem.*, **206,** 229 (1986).
11. I. Uchida, Y. Mugikura, T. Nishina, and K. Itaya, *ibid.*,

206, 241 (1986).
12. I. Uchida, T. Nishina, Y. Mugikura, and K. Itaya, *ibid.*, **209,** 125 (1986).
13. P. K. Adanuvor, R. E. White, and A. J. Appleby, *This Journal*, **137,** 2095 (1990).
14. T. Nishina, M. Takahashi, and I. Uchida, *ibid.*, **137,** 1112 (1990).
15. S. H. White and U. M. Twardoch, *ibid.*, **135,** 893 (1988).
16. H. Numata, H. Takagi, and S. Haruyama, in "Electrochemistry in Transition From the 20th to the 21th Century," B. E. Conway, O. J. Murphy, and S. Srinivasan, Editors, in press, Plenum Press, New York (1991).
17. C. Gabrielli, "Identification of Electrochemical Processes by Frequency Response Analysis," Solartron Electronic Group, Ltd. (1980).
18. R. De Levie and L. Pospísil, *J. Electroanal. Chem.*, **22,** 277 (1969).
19. E. Warburg, *Ann. Phys. Chem.*, **67,** 493 (1899).
20. J. E. B. Randles, *Discuss. Faraday Soc.*, **1,** 11 (1947).
21. B. Ershler, *ibid.*, **1,** 269 (1947).
22. M. Sluyters-Rehbach and J. H. Sluyters, in "Electroanalytical Chemistry," Vol. 4, A. J. Bard, Editor, p. 1, Marcel Dekker, New York (1970).
23. D. D. Macdonald and M. C. H. McKubre, in "Modern Aspects of Electrochemistry," Vol. 14, J. O'M. Bockris, B. E. Conway, and R. E. White, Editors, p. 61, Plenum Press, New York (1982).
24. J. R. Macdonald, *J. Electroanal. Chem.*, **223,** 25 (1987).
25. J. R. Macdonald, in "Impedance Spectroscopy-Emphasizing Solid Materials and Systems," J. R. Macdonald, Editor, p. 1, John Wiley & Sons, New York (1987).
26. J. R. Macdonald, *Electrochim. Acta*, **35,** 1483 (1990).
27. B. B. Davé, Ph.D. Dissertation, Texas A&M University, College Station, TX (1991).
28. J. R. Macdonald and L. D. Potter, Jr., *Solid State Ionics*, **23,** 61 (1987).
29. B. B. Dave, R. E. White, S. Srinivasan, and A. J. Appleby, *This Journal*, **138,** 673 (1991).
30. O. Levenspiel, "Chemical Reaction Engineering," p. 32, John Wiley & Sons, Inc., New York (1972).
31. A. Borucka, *This Journal*, **124,** 972 (1971).
32. S. H. Lu and J. R. Selman, *ibid.*, **137,** 1125 (1990).
33. R. S. Nicholson and I. Shain, *Anal. Chem.*, **36,** 706 (1964).
34. T. Berzins and P. Delahay, *J. Am. Chem. Soc.*, **75,** 555 (1953).

Electrochemical Impedance Studies of Hot Corrosion of Preoxidized Ni by a Thin-Fused Na_2SO_4 Film

Yiing Mei Wu*,[1] and Robert A. Rapp**

Department of Materials Science and Engineering, The Ohio State University, Columbus, Ohio 43210

ABSTRACT

A thin-film electrochemical arrangement has been developed to investigate the hot corrosion of preoxidized Ni by a fused Na_2SO_4 film at 1200 K in a catalyzed 0.1% SO_2-O_2 gas mixture. A Pt counterelectrode enables polarization measurements using the three-electrode configuration as well as open-circuit potentiometry. To extract mechanistic information without disturbing the system, the electrochemical impedance technique was used. Results of three distinct modes of hot corrosion (passive, pseudo-passive, and active) resulting from different preoxidation conditions are discussed.

The degradation of metals or alloys at elevated temperatures by a thin-fused salt film in the presence of an oxidizing gas is called hot corrosion. Several authors have proposed mechanisms for hot corrosion (1-7). The most widely discussed is the oxide fluxing model (4-11), by which oxide scales which are normally protective in gaseous oxidation are dissolved or penetrated by the molten salt. As discussed by Rapp (8, 9, 11), the solubility of a given oxide and the type of dissolution (acidic or basic) depend strongly on the basicity of the molten salt solvent. In the basic dissolution regime, where an oxide forms an anionic solute by complexing with oxide ions, its solubility is higher when the salt is more basic. The opposite is true in the acidic dissolution regime where the product solutes are cations and oxygen anions. When the dissolution of the scale is combined with a negative gradient for the oxide solubility in the salt film, caused by gradients in basicity or oxygen activity, the dissolved species migrate away from the dissolution site and reprecipitate within the salt film (7). Thus, a porous and nonprotective oxide is precipitated, and the compact adherent barrier oxide scale is destroyed. At this stage, direct contact between the metal and the salt film may produce sulfides and oxides, at least for attack by fused alkali sulfates. Formation of a sulfide locally depletes the sulfate melt of sulfur and thereby increases the melt basicity, perhaps significantly.

The electrochemical aspects of the metal-salt attack involved in hot corrosion can be divided into two half-cell reactions. The cathodic reduction reaction should generally be expected to create a condition of locally high basicity, with oxide ions as reaction products. If the salt film contains only a low concentration of transition metal ions, then the reduction of the oxidant species dissolved in the salt film must occur at the oxide/salt interface, where electrons are supplied directly from the metal oxidation reaction by inward hole migration through the oxide film. In turn, the arrival of the oxidant to the oxide/salt interface requires its dissolution and diffusion through the fused salt film. Since oxide dissolution and precipitation are also involved in the reaction sequence, the mechanism of hot corrosion, which includes diffusion, chemical and electrochemical reactions, is quite complicated.

Electrochemical methods such as scanning polarization, cyclic voltammetry, and chronopotentiometry have been employed in hot corrosion studies. Electrochemical impedance spectroscopy (EIS) is a technique which has proved effective in investigating reaction mechanisms and kinetics for other electrochemical phenomena. But successful application of the method requires suitable models for fitting the impedance data. Only a limited number of impedance investigations of hot corrosion, mostly preliminary work, have been reported. Farrell *et al.* (12) have employed electrochemical noise and impedance techniques to monitor the corrosion behavior of Nimonic 75 in bulk Na_2SO_4 and in Na_2SO_4/1% NaCl at 900 and 750°C. By comparing the impedance at a fixed low frequency (50 mHz), which was deliberately defined as the estimated polarization impedance Z_p, the authors concluded that the corrosion rate was higher at 900°C and with the addition of sodium chloride. The shape of the impedance diagrams also indicated a diffusion-controlled reaction, which results because of the separation of the specimen from the gaseous environment by a deep melt. Gao *et al.* (13) also used impedance and electrochemical noise techniques to monitor

* Electrochemical Society Student Member.
** Electrochemical Society Active Member.
[1] Present address: Mobil Research and Development Corporation, Paulsboro, New Jersey 08066-0486.